# Inorganic Chemistry Cite This: Inorg. Chem. 2019, 58, 1442–1450

pubs.acs.org/IC

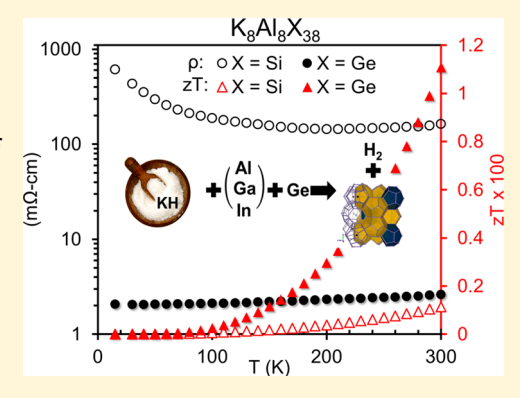
# Hydride Synthesis and Thermoelectric Properties of Type-I Clathrate $K_8E_8Ge_{38}$ (E = Al, Ga, In)

Christopher J. Perez, Victor J. Bates, and Susan M. Kauzlarich\*

Department of Chemistry, University of California, One Shields Avenue, Davis, California 95616, United States

Supporting Information

**ABSTRACT:** Type I clathrates of the composition  $K_8E_8Ge_{38}$  (E = Al, Ga, In) were prepared via the reaction of KH with E and Ge and thermoelectric properties measured in order to compare to K<sub>8</sub>Al<sub>8</sub>Si<sub>38</sub>, a promising thermoelectric material. The structures were confirmed with Rietveld refinement of powder diffraction patterns obtaining lattice parameters of 10.7729(2) Å, 10.7469(5) Å, and 10.9975(6) Å for E = Al, Ga, and In, respectively. Samples of  $K_8E_8Ge_{38}$  with E = Al and Ga were consolidated via spark plasma sintering for property measurements and determined to be 94.2% and 81.4% dense, respectively. K<sub>8</sub>In<sub>8</sub>Ge<sub>38</sub> showed significant decomposition after sintering with both elemental In and Ge present in the powder diffraction pattern. The thermoelectric properties of K<sub>8</sub>E<sub>8</sub>Ge<sub>38</sub> (E = Al, Ga) from 300-10 K were measured on sintered pellets. K<sub>8</sub>Al<sub>8</sub>Ge<sub>38</sub> was found to have a Seebeck coefficient, electrical resistivity, and thermal



conductivity of -35.8 μV/K, 2.56 mΩ cm, 1.37 W/m K at 300 K, respectively. K<sub>8</sub>Ga<sub>8</sub>Ge<sub>38</sub> was found to be a compensated semiconductor with a Seebeck coefficient, electrical resistivity, and thermal conductivity of 4.19  $\mu$ V/K, 1080 m $\Omega$ ·cm, and 1.05 W/m·K at 300 K, respectively. The resistivity of K<sub>8</sub>Al<sub>8</sub>Ge<sub>38</sub> is 46 times lower than K<sub>8</sub>Al<sub>8</sub>Si<sub>38</sub> which has a Seebeck coefficient of -90.0 µV/K and thermal conductivity of 1.77 W/mK at 300 K, suggesting that a solid solution of K<sub>8</sub>Al<sub>8</sub>Si<sub>38-x</sub>Ge<sub>x</sub> has potential for optimal thermoelectric performance.

#### 1. INTRODUCTION

Metal hydrides are useful reagents for preparing materials such as type-I clathrates, 1,2 the Ba<sub>1-x</sub>K<sub>x</sub>Fe<sub>2</sub>As<sub>2</sub> superconductor, 3 the promising thermoelectric material Mg<sub>2</sub>Si,<sup>4-7</sup> and others. Metal hydrides are fine, commercially available powders. Using powder reagents rather than the soft and sticky elemental group 1 or 2 metals helps with manipulating and mechanically milling these reagents with other elements into fine powders and can facilitate the scale-up of reactions.<sup>5</sup> The use of hydrides of group 1 and 2 metals was shown to make the synthesis of the Zintl phases Na<sub>4</sub>Si<sub>4</sub>, Na<sub>4</sub>Ge<sub>4</sub>, and K<sub>4</sub>Ge<sub>4</sub> more convenient.8 Metal hydrides decompose into their metal constituent and hydrogen which creates a reductive environment. A reductive environment is helpful when producing electronic materials because oxides that are typically insulating and can negatively influence electronic properties are either removed or inhibited from formation.5 Additionally, hydrides provide high surface area group 1 or 2 metals, which allow solid-state reactions to proceed faster and at lower temperatures.<sup>5,9</sup> There is no evidence of hydride incorporation in the materials described above.<sup>3,5</sup>

The type-I clathrate crystal structure was first discovered as a chlorine hydrate by Allen in 1959 (Figure 1). 10 A few years later inorganic sodium silicide clathrates were discovered by Kasper et al.<sup>11</sup> The complex unit cell of clathrate phases has gained attention for hydrogen storage, <sup>12,13</sup> thermoelectrics, <sup>14</sup> Li-ion batteries, <sup>15</sup> superconductors, <sup>16</sup> and many other applications. 17,18 The type-I clathrate structure (Figure 1) consists of a 20 vertex pentagonal-dodecahedron cage and a 24 vertex tetrakaidecahedron cage that form an extended covalent network. The framework encapsulates two unique guest host sites (referred to by their Wyckoff site notation as 2a and 6d) within each cage (Figure 1). The framework consists of group 14 elements (tetrel group) and can incorporate group 2, group 13, and group 15 elements as well as transition metals. 19 guest sites can be occupied by cationic group 1 or 2 elements that donate their electrons to the structure. In some cases, both group 1 and 2 elements can be incorporated as guests into the same structure.2 In frameworks that have tetrels and lower valent elements, the electrons donated by the cation are employed in covalent bonds. The wide variety of elements that can be used for the framework and guest sites make it possible to control the electronics of the structure. 18-20

Type-I clathrate phases have been studied for their application as superconductors, magnetocaloric coolers, photovoltaics, and thermoelectric materials that can convert heat directly into electricity. 17,19,21-24 When n-type and p-type semiconductors are placed electrically in series and thermally in parallel with a temperature gradient, the dominant charge carriers of the materials are driven toward the cold side in a phenomenon known as the Seebeck effect.<sup>25</sup> The Seebeck

Received: October 19, 2018 Published: December 27, 2018



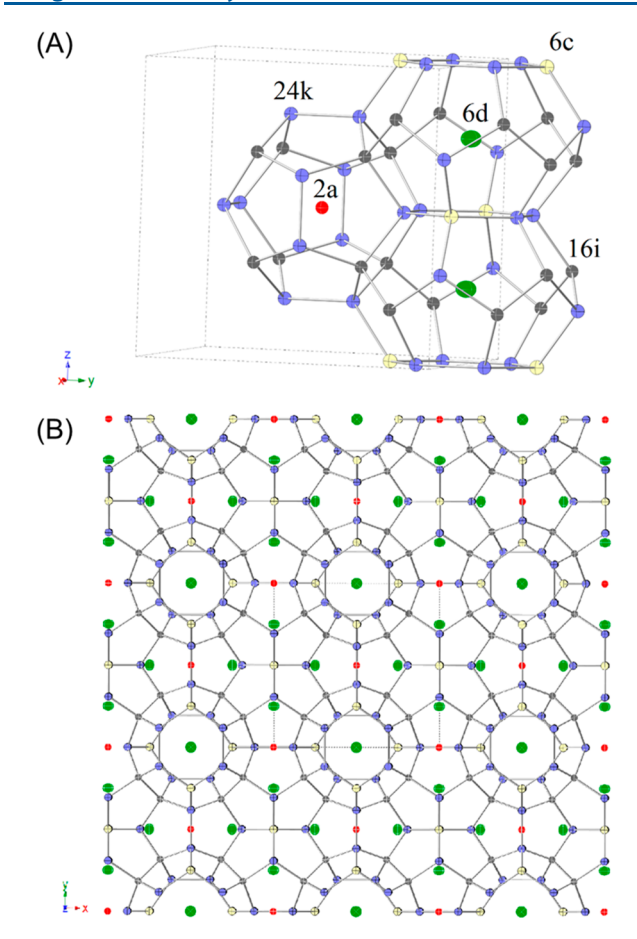


Figure 1. Views of the 20 vertex and 24 vertex cages of the type-I clathrate  $K_8Al_8Ge_{38}$  with Wyckoff sites colored and labeled: 2a, red; 6d, green; 6c yellow; 24k, blue; 16i, black. Thermal ellipsoid images of atoms are shown (90% probability) (A). Projection of the extended clathrate network (B).

effect generates a voltage that can be used to power devices. The efficiency of a thermoelectric material is defined by the unitless figure of merit,  $zT = \frac{\alpha^2}{\kappa \rho} T$ , where  $\alpha$  is the Seebeck coefficient,  $\rho$  is the electrical resistivity, T is the operating temperature, and  $\kappa$  is thermal conductivity. Ideal thermoelectric materials have been described as having glass-like thermal conductivity and crystal-like electrical conductivity, known as phonon glass electron crystal (PGEC) materials.<sup>2</sup> The diffuse covalent network of the type-I clathrate structure type allows for low electrical resistivity. 11 Clathrates have a low "glass-like" thermal conductivity which is proposed to originate from the guest atoms that are only loosely bound to the cages allowing for "rattling" (Umklapp scattering), leading to short phonon lifetimes and therefore low thermal conductivity.<sup>2</sup> Recently inelastic neutron scattering experiments on the type-I clathrates  $Ba_{7.81}Ge_{40.67}Au_{5.33}$  and  $Ba_8Ge_{40+x}Ni_{6-x}$  have shown phonon lifetimes and mean free paths that are far too large to support the hypothesis that isolated guest atoms are disrupting phonons by rattling. 28,29 This work has provided an alternative hypothesis pointing toward hybridization of the cage-guest phonon modes providing decreased thermal conductivity, making type-I clathrates ideal PGEC materials.<sup>29-31</sup>

NASA's Jet Propulsion Laboratory (JPL) estimates that if the existing US infrastructure were to be retrofitted with thermoelectric generators with average zT values between 1 and 2, up to 2.8 terawatt hours of power could be generated annually. Type-I clathrate  $K_8Al_8Si_{38}$  is a candidate for this application because it is made of earth-abundant, lightweight elements and is stable up to 810 °C.  $^{1,2,20}$  Moreover, at low temperatures, the  $\alpha$  and  $\kappa$  are similar to  $Ba_8Ga_{16}Ge_{30}$ , a type-I clathrate that is isoelectronic to  $K_8Al_8Si_{38}$  with a reported zT of 1.35 at 900 K.  $^{1,33,34}$  However,  $\rho$  of  $K_8Al_8Si_{38}$  is 200 times higher than  $Ba_8Ga_{16}Ge_{30}$  at 300 K.  $^{1,33,34}$ 

Replacing some Si with Ge should allow for higher mobility with the same carrier concentration, and this is a valid method for optimization of the thermoelectric properties; however, properties of the phase pure end members of K<sub>8</sub>E<sub>8</sub>Ge<sub>38</sub> (E = Al, Ga, In) have not yet been reported. Single crystal structures of the type-I clathrate  $K_8E_8Ge_{38}$  (E = Al, In)<sup>35,36</sup> have been reported, and lattice parameters from a crystal of K<sub>8</sub>Ga<sub>8</sub>Ge<sub>38</sub> have been reported.<sup>37</sup> Herein,  $K_8E_8Ge_{38}$  (E = Al, Ga, In) powders were synthesized with KH precursor, and the elements and characterized by powder X-ray diffraction (PXRD) in order to measure the thermoelectric properties. The composition of the dense pellets (94.2% for E = Al and 81.4% E = Ga) was characterized by electron microprobe wavelength dispersive spectroscopy (WDS). The thermostability of the materials was determined by differential scanning calorimetry (DSC), and the thermoelectric transport properties were measured.

## 2. EXPERIMENTAL SECTION

**2.1. Synthesis.** The synthesis of  $K_8E_8Ge_{38}$  (E = Al, Ga, In) was adapted from that reported for K<sub>8</sub>Al<sub>8</sub>Si<sub>38</sub>. Ge (99.999%, Furuchi Chem. Co., Japan) and E (Al shot, 99.99%, Furuchi Chem. Co., Japan; Ga ingots, 99.999%, Furuchi Chem. Co., Japan; In needles, 99.99%, Cerac) were weighed in air and arc-melted into ingots (total mass ~1.2 g) in an argon-filled arc welder. The ingots were crushed into ~50 mg pieces with a stainless steel mortar and pestle and placed into a 5 mL acrylic grinding vial (19.1 mm × 54 mm) with two Delrin end-caps, tungsten carbide inserts, and two 7.9 mm diameter tungsten carbide balls purchased from SPEX SamplePrep. Potassium hydride (KH, Sigma-Aldrich, 30 wt % dispersion in mineral oil), washed with toluene (dried in a solvent distiller) to remove the mineral oil and dried under vacuum, was added to the acrylic vial. The vial was closed, sealed in two airtight polyethylene bags, and mechanically milled for 30 min. To compensate for the experimentally observed loss of E and the vaporization of K, stoichiometry according to the formulas  $K_9Al_9Ge_{38}$ ,  $K_9Ga_9Ge_{38}$ , and  $K_9In_{8.5}Ge_{38}$  were used. The resulting black powders were placed in Nb tubes (Ta for In), arc-welded shut under argon, and jacketed in a fused silica tube under vacuum. The tubes were heated to 980 °C at a rate of 150 °C/h, held there for 10 h, and then cooled at 15  $^{\circ}$ C/h to 700  $^{\circ}$ C, where they were annealed for 40 h. The brittle condition of the Nb tubes after reaction suggests that KH produced hydrogen which reacted with niobium.<sup>38</sup> The tubes were opened in an argon-filled glovebox, and the products were fine black powders with some small annealed pieces.

Caution! KH is air and water reactive and should be handled in an inert atmosphere.

**2.2. Powder X-ray Diffraction.** The products were characterized by powder X-ray diffraction (PXRD). Diffraction patterns were taken with Cu K $\alpha$  radiation ( $\lambda$  = 1.5405 Å) on a Bruker D8 Eco Advance diffractometer operated at 40 kV and 40 mA at room temperature from 15° to 65° 2 $\theta$ . Rietveld refinement was performed with the JANA 2006 software package. The K<sub>8</sub>Al<sub>8</sub>Ge<sub>38</sub> and K<sub>8</sub>In<sub>8</sub>Ge<sub>38</sub> CIFs were used as the structural models for K<sub>8</sub>E<sub>8</sub>Ge<sub>38</sub> (E = Al, Ga) and K<sub>8</sub>In<sub>8</sub>Ge<sub>38</sub>, respectively. The following constraints were applied: (1) The composition determined from microprobe experiments was used to restrain the overall occupancy of K, E, and Ge for K<sub>8</sub>E<sub>8</sub>Ge<sub>38</sub> (E = Al, Ga); (2) E/Ge share x, y, z coordinates and isotropic temperature parameter  $B_{iso}$ ; (3) the profile shape was generated with a pseudo-Voigt function; (4) the background intensity was fitted using a shifted

10-order Chebyshev polynomial function; (5) the site occupancy for E/Ge was kept at 100% for each site; and (6) the relative occupancy of Al/Ge and In/Ge was refined. In the case of Ga/Ge, the refined experimental ratio of Al/Ge was employed as the model and the relative occupancy was not refined because there is not enough difference in scattering amplitude. The plotted data were normalized by dividing the observed and calculated data by the highest value in the observed set.

- **2.3. Spark Plasma Sintering.**  $K_8E_8Ge_{38}$  (E = Al, Ga, In) samples were consolidated by a Dr. Sinter Spark Plasma Sintering (SPS) System at 500 °C, 425 °C, and 425 °C, respectively, and 7.7 kN (613 MPa on the cross-section). 500 mg of the product was first ground and sieved (100 mesh), then loaded into 4 mm diameter graphite die with tungsten carbide plungers. The set up was placed into a larger 20 mm die with silicon carbide spacers and graphite plungers to accommodate for high-pressure sintering. The results were pellets ~8 mm thick with 94.2% density for E = Al and 81.4% for E = Ga. The In containing sample was not able to be consolidated without creating significant In and Ge impurities.
- **2.4. Thermoelectric Property Measurement.** Four mm pellets were cut into ~1 mm-thick disks with a diamond saw and polished flat and parallel to a mirror finish with silicon carbide polishing disks for thermoelectric measurements. Thermal conductivity and Seebeck coefficients were measured with the thermal transport option (TTO) of Quantum Design Physical Property Measurement System (PPMS). Two gold-coated copper leads were attached to the top and bottom of the sample with conductive silver epoxy for measurement. Resistivity measurements were done with the alternating current (AC) transport option of the PPMS, where the sample was mounted on a puck, with four platinum leads attached to the surface of the samples with silver paint.
- **2.5. Differential Scanning Calorimetry (DSC).** The thermal stability of K<sub>8</sub>E<sub>8</sub>Ge<sub>38</sub> (E = Al, Ga, In) was determined by DSC employing a Netzsch Thermal Analysis STA 409 PC. Approximately 20 mg of powder was flame-sealed into an evacuated fused silica tube and placed in the DSC sample holder. The samples were scanned under flowing argon at 10 °C/min, both increasing and decreasing temperature, in three different runs to 1000 °C, 900 °C, and 900 °C. Additionally, approximately 50 mg of K<sub>8</sub>E<sub>8</sub>Ge<sub>38</sub> (E = Al, Ga) sintered pellet (E = In was a hand pressed powder) was placed in an alumina crucible, and data were collected at 10 °C/min, both increasing and decreasing temperature, under flowing argon to 650 °C, 550 °C, and 600 °C, respectively. Heating and cooling data were also collected to 220 °C and 550 °C for sintered pellet samples of K<sub>8</sub>Al<sub>8</sub>Ge<sub>38</sub>. The onset of features was determined by Netzsch Proteus analysis software.
- **2.6. Electron Microprobe Characterization.** Elemental analysis and mapping of  $K_8E_8Ge_{38}$  (E = Al, Ga) was performed on polished sintered pellets with a Cameca SX-100 electron microprobe equipped with five wavelength-dispersive spectrometers. The  $K\alpha$  of K was standardized from an orthoclase standard,  $K\alpha$  of Al from an alumina standard, and  $L\alpha$  of Ge from germanium single crystal standard. The stoichiometry of  $K_8Al_8Ge_{38}$  was averaged from three data points, and  $K_8Ga_8Ge_{38}$  was averaged from 15 data points.
- **2.7. Carrier Concentration.** Hall measurements and electrical resistivity were measured on sintered pellets using the home-built Van der Pauw set up at JPL with tungsten pressure contacts and a 0.8 T magnet, as described herein.<sup>40</sup>

# 3. RESULTS AND DISCUSSION

**3.1. PXRD and Rietveld Refinement.**  $K_8E_8Ge_{38}$  (E = Al, Ga, In) samples were prepared by a reaction of the ball milled mixture of KH with E + Ge that was arc-melted into a pellet. The stoichiometry employed in the reaction provided an excess of K and E according to the following compositions:  $K_9Al_9Ge_{38}$ ,  $K_9Ga_9Ge_{38}$ , and  $K_9In_{8.5}Ge_{38}$ . Samples with lower amounts of E showed peaks corresponding to Ge in the powder diffraction. Figure 2 shows the powder diffraction data

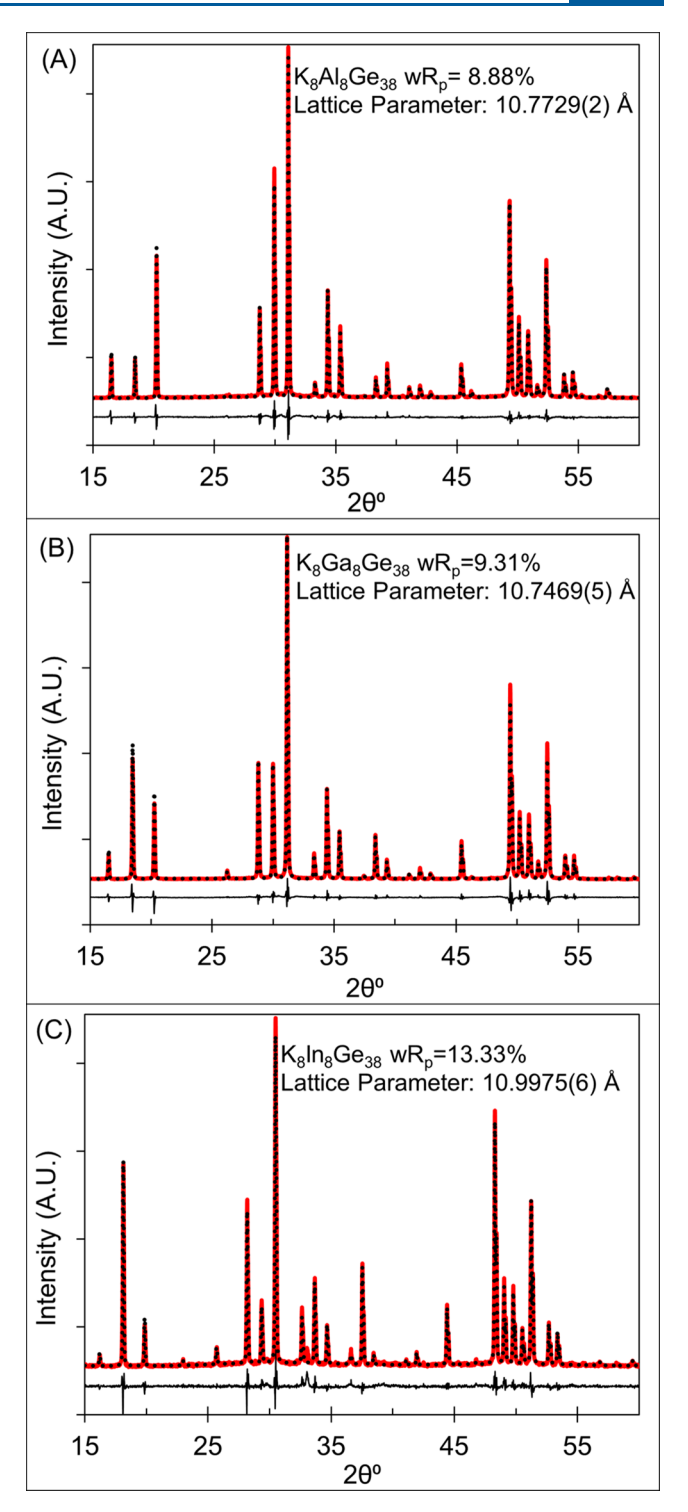


**Figure 2.** A portion of the powder diffraction pattern showing the Rietveld refinement of  $K_8Al_8Ge_{38}$  (A),  $K_8Ga_8Ge_{38}$  (B), and  $K_8In_8Ge_{38}$  (C) with the observed pattern in red, calculated pattern dotted, and the difference between calculated and observed as a solid below the data.

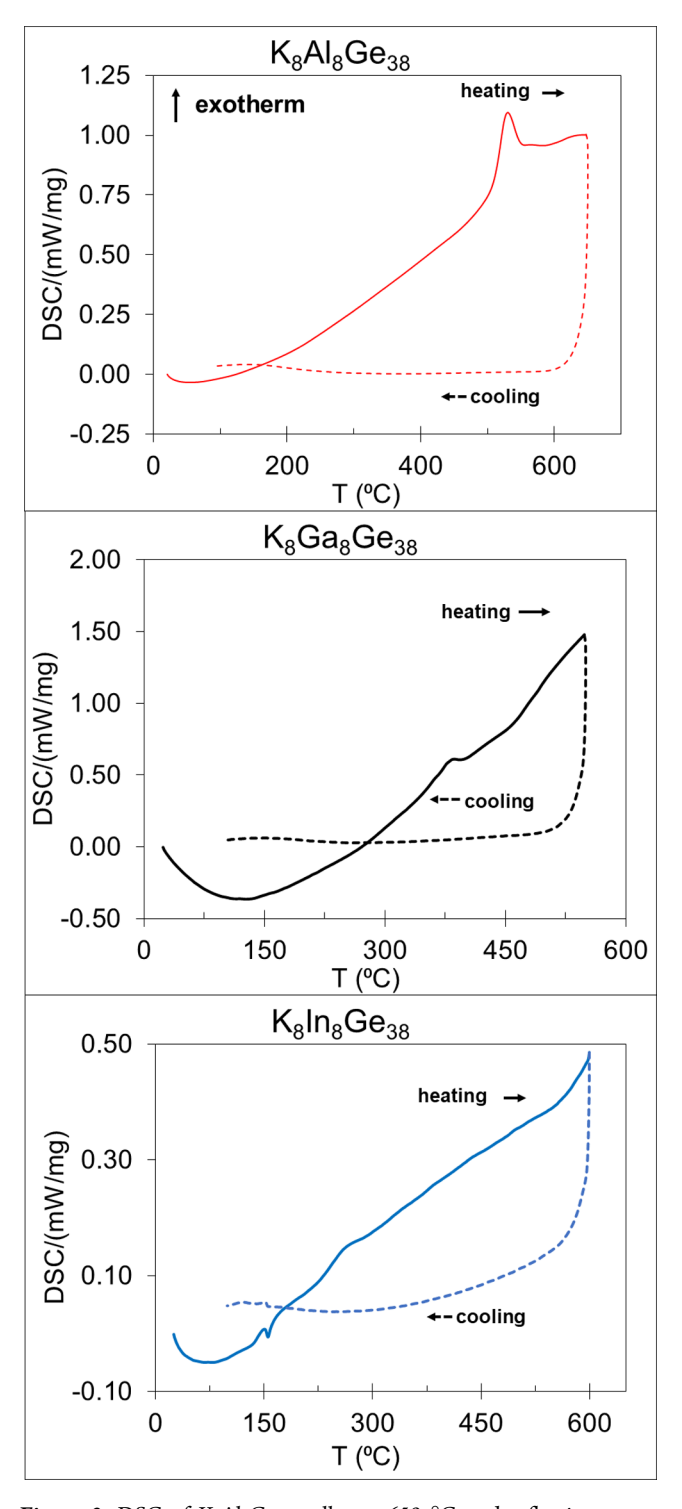
and Rietveld refinement for  $K_8E_8Ge_{38}$  (E = Al, Ga, In) before consolidation. The refinement confirmed that  $K_8E_8Ge_{38}$  (E = Al, Ga, In) crystallizes in the cubic space group Pm3n of type-I clathrate structure-type. The Rietveld refinement parameters for the samples are indicated with the residuals provided below the diffraction data. Rietveld refinement of the  $K_8Ga_8Ge_{38}$  samples was performed starting with the crystallographic file

Table 1. Rietveld Refinement Results of  $K_8E_8Ge_{38}$  (E = Al, Ga, In) and Reported Lattice Parameters from Single Crystals

parameter				comment		
nominal formula			K <sub>8</sub> Al <sub>8</sub> Ge <sub>38</sub>	K <sub>8</sub> Ga <sub>8</sub> Ge <sub>38</sub>		K <sub>8</sub> In <sub>8</sub> Ge <sub>38</sub>
space group			0 0 30	$Pm\overline{3}n$		0 0 30
reported lattice constant (Å) <sup>35-37</sup>			10.785(1)	10.7706(5)		10.9975(6)
prepre-SPS			10.7729(2)	10.7469(5)		10.9975(6)
lattice constant (Å)						
post-SPS			10.7732(8)	10.7468(4)		10.9966(4)
	onstant (Å)					
pre-SPS (Rp, wRp)			6.27%, 8.88%	6.02%, 9.31%		9.69%, 13.33%
post-SPS (Rp, wRp)			8.84%, 12.42%	7.94%, 11.47%		8.89%, 13.78%
site	occupancy		ADP $(Å^2)$			(x, y, z)
$(K_8Al_8Ge_{38})$						
2a (K)	100%	0.013(3)			0, 0, 0	
6d (K)	96.2(4) %	$U_{11} = 0.018(4); U_{22} = U_{33} = 0.011(2)$			1/4, 1/2, 0	
6c (E)	95.2(6) %	0.005(3)			1/4, 0, 1/2	
16i (E)	6.3(1) %	0.002(1)			0.1835(8), $x$ , $x$	
24k (E)	3.6(2) %	0.0072(6)			0, 0.3076(1), 0.1174(1)	
$(K_8Ga_8Ge_{38})$						
2a (K)	100%	0.013(4)			0, 0, 0	
6d (K)	93(1) %	$U_{11} = 0.011(5); U_{22} = U_{33} = 0.025(3)$			1/4,	1/2, 0
6c (E)	$6c  ext{ (E)}  ext{ 0.01(1)}$				1/4, 0, 1/2	
16i (E)	16i (E) 0.01(2)				0.1840(8), $x$ , $x$	
24 <i>k</i> (E)					0, 0.307(1), 0.1178(9)	
$(K_8In_8Ge_{38})$						
2a (K)	100%	0.068(7		0, 0, 0		
6d (K)	100%	$U_{11} = 0$ 0.064	$J_{33} =$	1/4, 1/2, 0		
6c (E)	84(2) %	0.011(2)			1/4, 0, 1/2	
16i (E)	3(1) %	0.016(2)			0.183(1), x, x	
24 <i>k</i> (E)	5(1) %	0.014(2)				302(2), .115(2)

(CIF) of the published  $K_8Al_8Ge_{38}^{\ 35}$  structure with Ga replacing Al because  $K_8Ga_8Ge_{38}$  does not have a CIF available in the International Crystallographic Structure Database. For  $K_8Al_8Ge_{38}$  and  $K_8Ga_8Ge_{38}$ , the refinement is consistent with phase purity before SPS consolidation. Rietveld refinement indicates that  $K_8In_8Ge_{38}$  shows a small amount (<1% by weight) of In impurity at  $33.0^\circ.$ 

Table 1 provides the lattice constants from reported single crystal data<sup>35–37</sup> and those obtained from Rietveld refinement of the samples described herein. The as-prepared  $K_8Al_8Ge_{38}$  and  $K_8Ga_8Ge_{38}$  have lattice constants 10.7729(2) Å and 10.7469(5) Å, respectively, slightly smaller compared to the published single crystal data of the same nominal compositions, 10.785(1) Å and 10.7706(5) Å.<sup>35,37</sup>  $K_8In_8Ge_{38}$  has lattice parameters similar to the published ones.<sup>42</sup> There is little difference in the lattice parameters of the as-made vs consolidated pellets for all samples. However, since a high-quality dense pellet of  $K_8In_8Ge_{38}$  could not be prepared, further characterization was not performed. The stoichiometry of the dense pellets of the E = Al, G a samples was calculated to be  $K_{7.8(1)}Al_{7.69(9)}Ge_{38.5(1)}$  and  $K_{7.64(4)}Ga_{7.81(3)}Ge_{38.54(6)}$  from WDS data. The slightly smaller lattice constants observed for



**Figure 3.** DSC of  $K_8Al_8Ge_{38}$  pellet to 650 °C under flowing argon,  $K_8Ga_8Ge_{38}$  pellet to 550 °C under flowing argon, and  $K_8In_8Ge_{38}$  pressed powder to 600 °C. A gain in signal indicates an exothermic process, a loss of signal indicates an endothermic process. Heating (solid) and cooling (dashed) data are shown.

these samples are attributed to K or Al deficiencies in the structure. Elemental mapping of the pellets is provided in Supporting Information (SI).

The as-prepared powders were consolidated into 4 mm diameter pellets via SPS. Temperature and pressure profiles were investigated to obtain high-density pellets.  $K_8E_8Ge_{38}$  (E = Al, Ga, In) was pressed at 500 °C, 425 °C, and 425 °C,

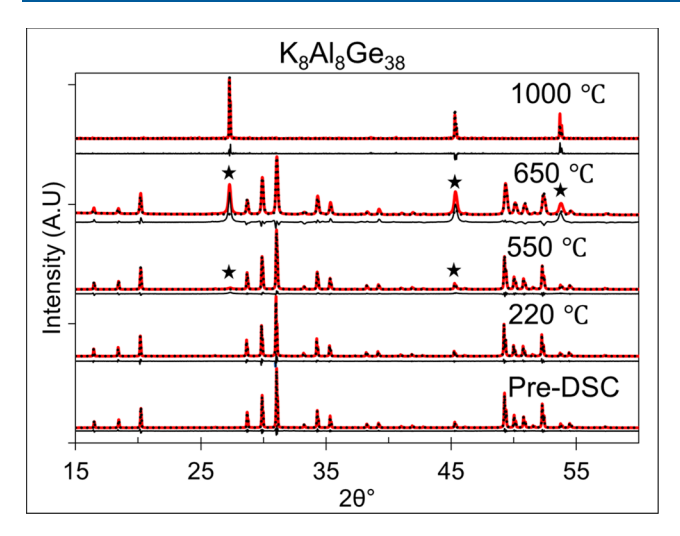


**Figure 4.** PXRD before and after DSC cycled to 220 °C, 550 °C, 650 °C, and 1000 °C for  $K_8Al_8Ge_{38}$ . The red line indicates the observed pattern, the black dotted line represents the simulated pattern, and the black solid line is the difference between observed and calculated. Black stars denote peaks from Ge. Rietveld refinement of scans obtained at 1000 °C was performed employing the Ge CIF. <sup>43</sup>

respectively, with 7.7 kN of force (613 MPa on the cross section). Post-SPS consolidation PXRD patterns with Rietveld refinement are provided in SI. After SPS, broadening of the peaks can be observed in all three samples, indicating strain from the high pressure applied. After SPS, two small impurity peaks appear in the powder diffraction pattern at 34.9° and  $40.5^{\circ}$  for  $K_8E_8Ge_{38}$  (E = Al, Ga). These are unidentified side phases of low concentration, presumably a result of slight decomposition from the high-temperature processing into the dense pellet. Lower pressures and temperatures employed in the SPS lead to densities <80%, therefore, the small amount of impurity was considered acceptable for property measurements. Since the impurity is consistent in both samples of  $K_8E_8Ge_{38}$  (E = Al, Ga), comparison of transport data of the samples provides valid insight into the properties. In the case of K<sub>8</sub>Ga<sub>8</sub>Ge<sub>38</sub>, after SPS an additional peak at 27.3°, assigned to Ge is observed (<0.5% by weight). Post SPS K<sub>8</sub>In<sub>8</sub>Ge<sub>38</sub> shows two small unknown impurity peaks at 26.6° and 21.5° and additional peaks assigned to Ge and In. Rietveld refinement of the mixture indicates the weight % to be 92.7% K<sub>8</sub>In<sub>8</sub>Ge<sub>38</sub>, 2.8% In, and 4.5% Ge. Therefore, the transport properties of the K<sub>8</sub>In<sub>8</sub>Ge<sub>38</sub> pellet were not measured, as the inclusion of both elemental In and Ge in the final pellet was high enough to make the determination of the intrinsic properties of K<sub>8</sub>In<sub>8</sub>Ge<sub>38</sub> difficult and the interpretation highly suspect. Pressing K<sub>8</sub>In<sub>8</sub>Ge<sub>38</sub> at lower temperatures lead to less dense pellets, and pressing at higher pressures disintegrated the graphite SPS die to the point where a pellet could not be recovered.

**3.2. Thermal Stability.** DSC was used to determine the stability of  $K_8E_8Ge_{38}$  (E = Al, Ga, In) with cycling from room temperature to 1000 °C, 900 °C, and 900 °C respectively (SI).  $K_8E_8Ge_{38}$  (E = Al, Ga) samples were also scanned to 550 °C, and  $K_8In_8Ge_{38}$  was scanned to 600 °C to amplify features seen in higher temperature scans.  $K_8Al_8Ge_{38}$  was also scanned to 220 °C (SI).

Figure 3 provides the DSC scans of  $K_8Al_8Ge_{38}$  to 650 °C,  $K_8Ga_8Ge_{38}$  pellet to 550 °C, and  $K_8In_8Ge_{38}$  pressed powder to 600 °C. The DSC scan of  $K_8Al_8Ge_{38}$  shows the onset of an

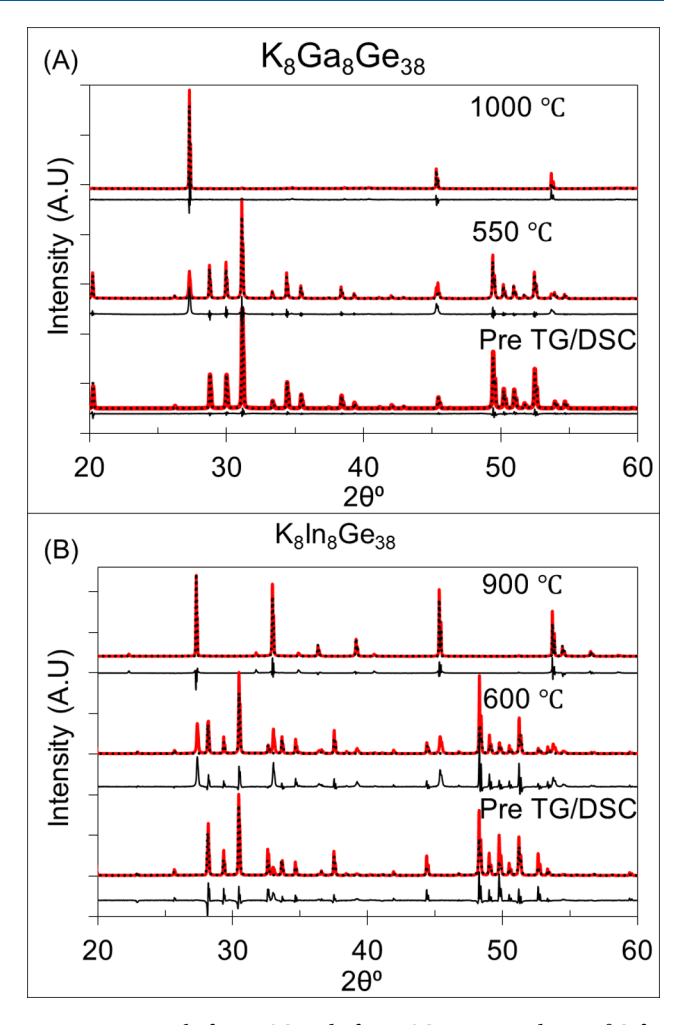


**Figure 5.** PXRD before DSC and after DSC to 550 and 1000  $^{\circ}$ C for  $K_8Ga_8Ge_{38}$  (A) and before and after DSC to 600 and 900  $^{\circ}$ C for  $K_8In_8Ge_{38}$  (B). The red line represents the observed pattern, the black dotted line represents the simulated pattern, and the black solid line represents the difference between observed and calculated. Rietveld refinement of scans obtained at 900  $^{\circ}$ C was performed employing the Ge CIF.  $^{43}$ 

exothermic peak at 509 °C attributed to the decomposition of the clathrate.  $K_8Ga_8Ge_{38}$  shows a similar feature at 360 °C which is attributed to the exothermic decomposition.  $K_8In_8Ge_{38}$  with  $\sim\!1\%$  In impurity shows an endothermic peak at 149 °C which corresponds to the melting of In. There is an additional exothermic peak with an onset at 240 °C which is attributed to the decomposition of the  $K_8In_8Ge_{38}$  clathrate structure.

Figure 4 shows the PXRD data for the  $K_8Al_8Ge_{38}$  DSC sample after cycling to the temperature indicated in the plot along with the refinement fits and residuals. The PXRD pattern after DSC to 220 °C shows no change from the pre-DSC scan, indicating the structure is stable up to this temperature. After DSC to 550 and 650 °C, a diffraction peak at  $2\theta = 27.3^{\circ}$  appears (indicated with a star) which can be refined as 3.3% and 20% Ge by weight, respectively. The increasing amount of Ge with increasing temperature suggests that some of the sample has decomposed at 550° and significantly more at 650°C, consistent with the assignment of the exothermic peak at 509 °C in the DSC scan to the decomposition of the sample. PXRD after DSC to 1000 °C shows only Ge remaining.

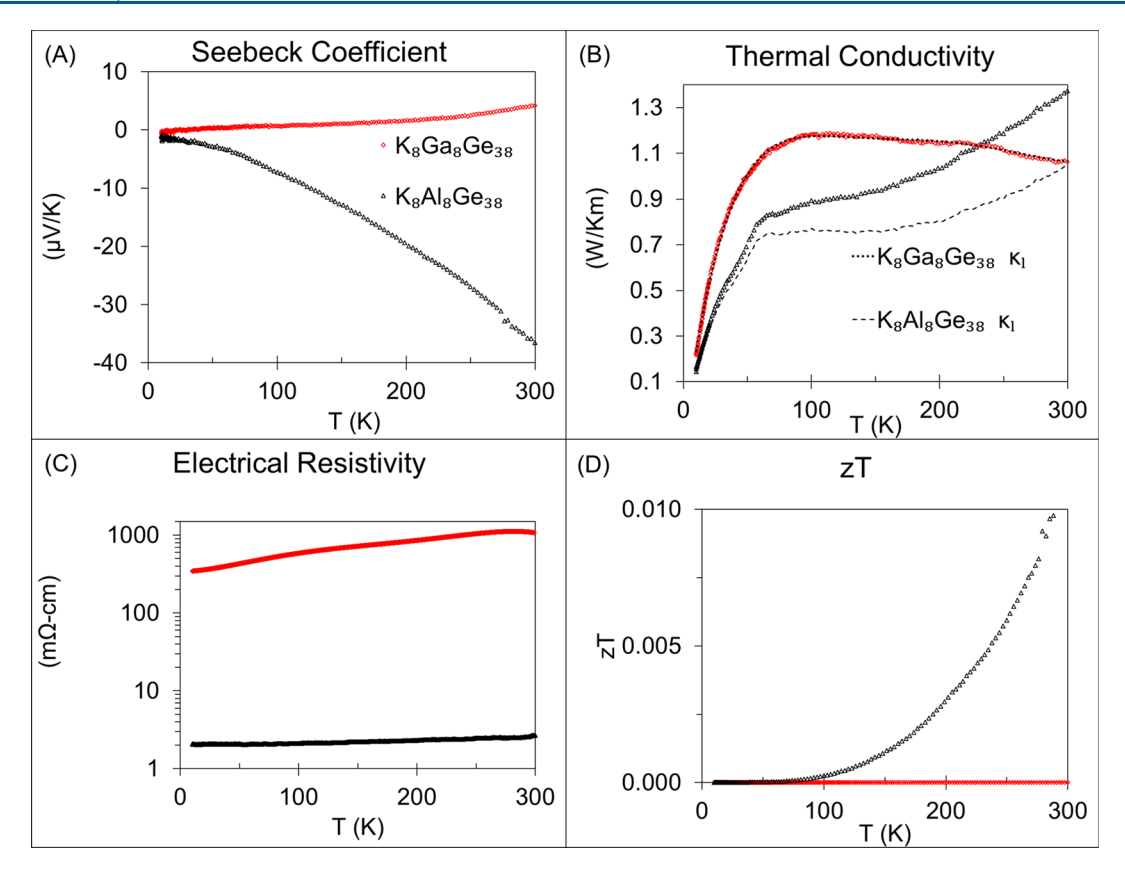
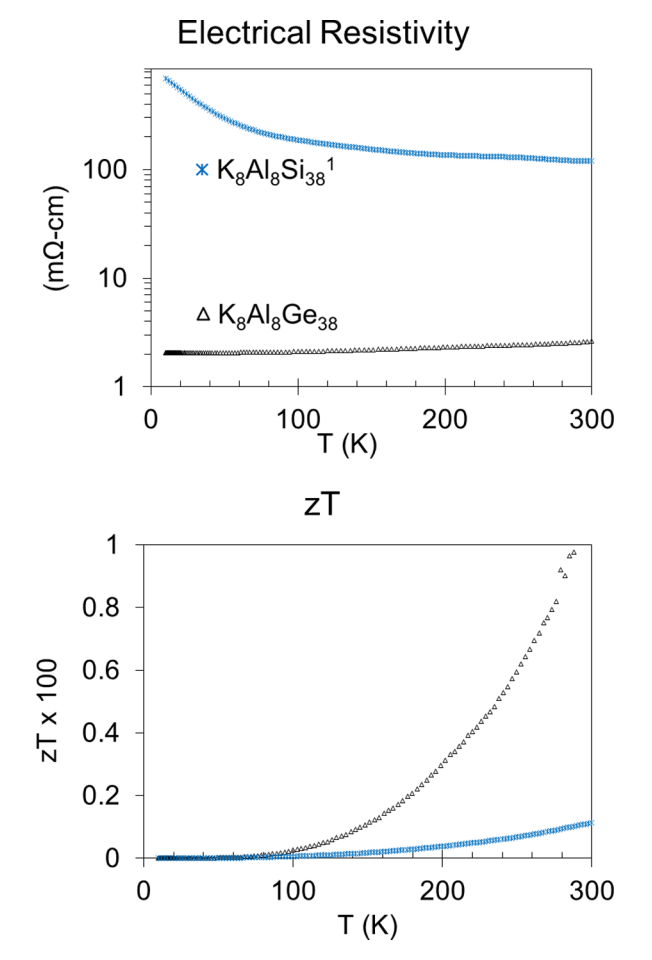


Figure 6. Low-temperature thermoelectric properties of  $K_8Al_8Ge_{38}$  (black triangles) and  $K_8Ga_8Ge_{38}$  (red diamonds). Seebeck coefficient measured with the TTO option on a PPMS (A). Thermal conductivity measured with the TTO option on a PPMS with the lattice thermal conductivity labeled with dashed lines (B). Electrical resistivity measured with a four probe AC resistivity set up on a PPMS (C) and calculated zT (D).

Figure 5 shows the PXRD data for  $K_8E_8Ge_{38}$  (E = Ga, In) after DSC to the stated temperature, their fits, and residuals. The PXRD of K<sub>8</sub>Ga<sub>8</sub>Ge<sub>38</sub> after DSC up to 550 °C shows the growth of a peak at  $2\theta = 27.3^{\circ}$  which was refined to 10.6% Ge by weight, indicating that this structure starts to decompose at 360 °C where the exothermic peak is seen in the DSC scan. PXRD after DSC to 900 °C (SI) shows only Ge remaining. PXRD of K<sub>8</sub>In<sub>8</sub>Ge<sub>38</sub> after DSC to 600 °C shows 18.0% Ge by mass and 5.4% In by mass by Rietveld refinement, indicating that the structure has begun to decompose at the initial upturn in the DSC signal seen at 240 °C. PXRD after DSC scan to 900 °C shows Ge and In remaining along with some stray peaks that can be attributed to the fused silica container reacting with the sample, indicating that when heated to 900 °C the sample completely decomposes. These structures do not immediately decompose, but slowly begin to lose K and E when taken above their decomposition temperature.

**3.3. Low-Temperature Thermoelectric Properties.** SPS was used to consolidate  $K_8E_8Ge_{38}$  (E = Al, Ge) powders into pellets with densities of 94% and 81%, respectively. Figure 6 shows the Seebeck coefficient, thermal conductivity, electrical resistivity, and zT for the samples from 300 - 2 K. At 300 K, the Seebeck for  $K_8Al_8Ge_{38}$  is  $-35.8~\mu\text{V/K}$ , indicating that it is an n-type semiconductor. The thermal conductivity,  $\kappa$ , is 1.37 W/mK at 300 K. The line shape of the thermal conductivity (Figure 6B) deviates from the Callaway model for lattice thermal conductivity ( $\kappa_l$ ), indicating a large contribution from the electronic portion of thermal conductivity ( $\kappa_e$ ) to the overall thermal conductivity ( $\kappa_{tot}$ ). The Wiedemann–Franz law ( $\kappa_{tot} = \kappa_e + \kappa_l$ ,  $\kappa_e = L\sigma T$ ), where L is the Lorentz value

calculated from  $L=(1.5+{\rm e}^{-(\frac{S}{116})})\times 10^{-8}\frac{W}{K^2\Omega}$ , and S is the Seebeck coefficient in  $\mu V/K$ , was used to calculate the lattice thermal conductivity, which is plotted in Figure 6B. It can be seen that as temperature increases, less of the thermal conductivity is attributed to the lattice portion, indicating the material has a high carrier concentration and confirms that  $\kappa_{\rm e}$ contributes significantly to  $\kappa_{\text{tot}}^{25}$  The resistivity of  $K_8Al_8Ge_{38}$ (Figure 6C) was 2.56 m $\Omega$ ·cm at 300 K, lower than the published value of 370 m $\Omega$ ·cm at 300 K which was measured on a single crystal sample of K<sub>8</sub>Al<sub>8</sub>Ge<sub>38</sub>. Simple electron counting for the clathrate structure provides K as the electropositive element donating electrons to the framework consisting of Al and Ge. All framework atoms are 4-bonded (tetrahedral), so the Al requires an additional electron to make a fourth bond. Microprobe data show that there is slightly more K than Al present  $(K_{7.8(1)}Al_{7.69(9)}Ge_{38.5(1)})\text{, so there}$ should be an excess of electrons, making the typically semiconducting  $K_8Al_8Ge_{38}$  (375 m $\Omega$ ·cm)<sup>35</sup> closer to a degenerate semiconductor.<sup>17</sup> Imai et al. show a similar behavior in  $K_8Al_7Si_{39}$  where the resistivity at 300 K is 8 m $\Omega$ · cm, much lower than 120 m $\Omega$ ·cm that was reported for  $K_8Al_8Si_{38}$ . The zT at 300 K for  $K_8Al_8Ge_{38}$  (Figure 6D) of 0.011 is a 10-fold improvement over K<sub>8</sub>Al<sub>8</sub>Si<sub>38</sub> which has a zT of 0.0011 (Figure 7). The increase in zT over K<sub>8</sub>Al<sub>8</sub>Si<sub>38</sub> is attributed to the large reduction in electrical resistivity (as shown) and a small decrease of thermal conductivity compared to the values for  $K_8Al_8Si_{38}$  at 300 K of 120 m $\Omega$ ·cm and 1.77 W/mK, respectively. These differences are large enough in magnitude to offset the reduction in Seebeck from  $-90.0 \,\mu\text{V}/$ K for  $K_8Al_8Si_{38}$  to  $-35.8 \mu V/K$  for  $K_8Al_8Ge_{38}$ . For



**Figure 7.**  $K_8Al_8Ge_{38}$  shows a 10-fold improvement in zT over  $K_8Al_8Si_{38}$  that can be attributed to a large reduction in electrical resistivity. Data for  $K_8Al_8Si_{38}$  are from ref 1.

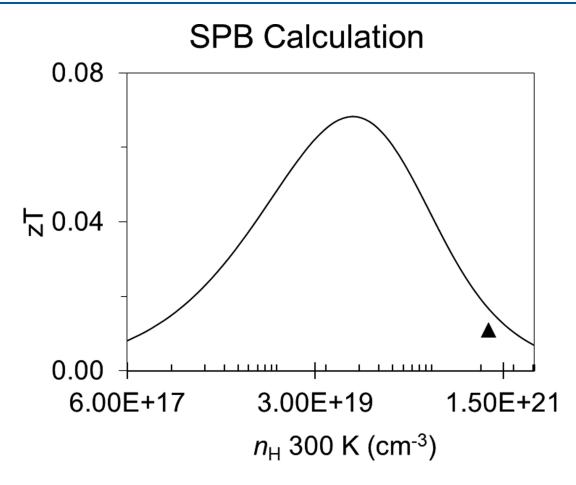


Figure 8. SPB model calculations of zT vs carrier concentration (300 K) with a zT maxima at  $6.32 \times 10^{19} \text{ cm}^{-3}$  plotted with the measured zT of  $K_8Al_8Ge_{38}$ .

comparison,  $K_8Al_7Si_{39}$  has values of 8 m $\Omega$ ·cm, 1.72 W/mK, -65.5  $\mu$ V/K, and 0.0096 for resistivity, thermal conductivity, Seebeck, and zT at 300 K, respectively.<sup>45</sup>

The Seebeck coefficient of  $K_8Ga_8Ge_{38}$  at 300 K is 4.19  $\mu$ V/K indicating a p-type semiconductor, consistent with the stoichiometry  $K_{7.64(4)}Ga_{7.81(3)}Ge_{38.54(6)}$  (Figure 6A). The thermal conductivity shows an increase followed by a

downturn at 100 K following the Callaway model for lattice thermal conductivity and has a value of 1.06 W/mK at 300 K (Figure 6B).  $^{44}$   $\kappa_l$  was calculated with the Wiedemann–Franz law as described above and is plotted in Figure 6B.  $\kappa_l$  shows no difference from  $\kappa_{tot}$  indicating the sample has a low amount of charge carriers, and the thermal conductivity arises mostly from lattice contributions.  $^{44}$  The resistivity is 1080 m $\Omega \cdot$ cm at 300 K which is much higher than the  $K_8Al_8Ge_{38}$  sample. The zT is  $1.93 \times 10^{-6}$  because of the high resistivity and low Seebeck coefficient.

3.4. Carrier Concentration and Single Parabolic Band (SPB) Model. A carrier concentration of  $1.083(1) \times 10^{21}$  cm<sup>-3</sup> and a mobility of 3.725(3) cm<sup>2</sup>/V·s were measured at room temperature for  $K_8Al_8Ge_{38}$  compared to  $1.31 \times 10^{18}$  cm<sup>-3</sup> and a mobility of  $\sim 39 \text{ cm}^2/\text{V} \cdot \text{s}$  for  $K_8 \text{Al}_8 \text{Si}_{38}$ , as a result  $K_8 \text{Al}_8 \text{Ge}_{38}$ has a much lower resistivity and Seebeck coefficient.<sup>21</sup> Hall measurements of K<sub>8</sub>Ga<sub>8</sub>Ge<sub>38</sub> gave positive and negative charge carrier values suggesting the material is a compensated semiconductor, so the data were not used for SPB calculations (SI). The SPB model has been shown to do an adequate job predicting thermoelectric properties of type-I clathrates.<sup>4</sup> Calculations were performed following typical procedures described in the literature. 47,48 SPB calculations (Figure 8) provide an estimate of a zT of 0.017 at  $1.083(1) \times 10^{21}$  cm<sup>-3</sup> for K<sub>8</sub>Al<sub>8</sub>Ge<sub>38</sub>, which is slightly higher than the measured value of 0.011. SPB overestimates the thermal conductivity of the material (1.50 W/mK vs 1.36 W/mK) and underestimates the electrical resistivity (1.57m $\Omega$ ·cm vs 2.56 m $\Omega$ ·cm), which is explained by the high amount of grains seen in the electron microprobe image which will elevate resistivity and lower thermal conductivity (SI). Calculations indicate that a K<sub>8</sub>Al<sub>8</sub>Ge<sub>38</sub> clathrate with a charge carrier concentration of  $6.32 \times 10^{19}$  cm<sup>-3</sup> would have a zT of 0.067 at 300 K as suggested by Figure 8. Other thermoelectric Zintl phases show peak thermoelectric performance at carrier concentrations of  $10^{19}-10^{20}$  cm<sup>-3</sup> as well. Reducing carrier concentration can be achieved by doping the structure with Zn or Mg in place of Al or through better control of the relative stoichiometry of K and Al.

#### 4. SUMMARY

This work provides a synthetic route and consolidation profile to make dense pellets of K<sub>8</sub>E<sub>8</sub>Ge<sub>38</sub> (E = Al, Ga). Decomposition is initiated at 509 °C, 360 °C, and 240 °C for  $K_8E_8Ge_{38}$  (E = Al, Ga, In), respectively. Thermoelectric properties were not measured on K<sub>8</sub>In<sub>8</sub>Ge<sub>38</sub> because it could not be consolidated into a dense pellet without additional impurities. K<sub>8</sub>Ga<sub>8</sub>Ge<sub>38</sub> showed poor thermoelectric performance as a compensated semiconductor. The thermoelectric properties of K<sub>8</sub>Al<sub>8</sub>Ge<sub>38</sub> show a significant improvement over K<sub>8</sub>Al<sub>8</sub>Si<sub>38</sub>. These results suggest that measuring the hightemperature thermoelectric properties of K<sub>8</sub>Al<sub>8</sub>Ge<sub>38</sub>, better stoichiometric control of K<sub>8</sub>Al<sub>8</sub>Ge<sub>38</sub>, and a solid solution of K<sub>8</sub>Al<sub>8</sub>Si<sub>38-x</sub>Ge<sub>x</sub>, may lead to a promising zT. Also, the lack of a Ge-Si eutectic point suggests a K<sub>8</sub>Al<sub>8</sub>Si<sub>38-x</sub>Ge<sub>x</sub> solid solution may be stable between the decomposition temperature of K<sub>8</sub>Al<sub>8</sub>Si<sub>38</sub> (810 °C) and K<sub>8</sub>Al<sub>8</sub>Ge<sub>38</sub> (509 °C) providing a material that can operate on a vehicle's exhaust system (250-750 °C) or other industrial processes. <sup>2,53-55</sup> In addition to Si-Ge alloying, other elements such as with Zn or Mg can be incorporated in order to reduce the carrier concentration and may provide a successful direction toward a high zT.

#### ASSOCIATED CONTENT

#### **S** Supporting Information

The Supporting Information is available free of charge on the ACS Publications website at DOI: 10.1021/acs.inorg-chem.8b02977.

Topological and back scattered electron Z-contrast images of  $K_8Al_8Ge_{38}$  and  $K_8Ga_8Ge_{38}$ ; post SPS PXRD of  $K_8Al_8Ge_{38}$ ,  $K_8Ga_8Ge_{38}$ , and  $K_8In_8Ge_{38}$ ; additional DSC scans of  $K_8Al_8Ge_{38}$ ,  $K_8Ga_8Ge_{38}$ , and  $K_8In_8Ge_{38}$ ; and Hall carrier concentration plots for  $K_8Al_8Ge_{38}$  and  $K_8Ga_8Ge_{38}$  (PDF)

# AUTHOR INFORMATION

#### **Corresponding Author**

\*E-mail: smkauzlarich@ucdavis.edu.

ORCID ®

Christopher J. Perez: 0000-0002-1088-0190 Susan M. Kauzlarich: 0000-0002-3627-237X

Notes

The authors declare no competing financial interest.

#### ACKNOWLEDGMENTS

This research was sponsored by NSF (DMR-1405973, 1709382). The authors thank Kasey Devlin for DSC and PXRD measurements, Jackson Badger and Valentine Taufour (UC Davis Physics) for AC resistivity measurements, and Nicholas Botto for assistance with microprobe analysis. The authors acknowledge Kirill Kovnir for access to the PPMS. The authors thank Václav Petricek and Fan Sui for helpful discussion on Rietveld refinement and synthesis. Part of this work was conducted at the Jet Propulsion Laboratory/ California Institute of Technology under contract with the National Aeronautics and Space Administration with funding from the Science Mission Directorate's Radioisotope Power Systems program.

## REFERENCES

- (1) Sui, F.; He, H.; Bobev, S.; Zhao, J.; Osterloh, F. E.; Kauzlarich, S. M. Synthesis, Structure, Thermoelectric Properties, and Band Gaps of Alkali Metal Containing Type I Clathrates:  $A_8Ga_8Si_{38}$  (A = K, Rb, Cs) and  $K_8Al_8Si_{38}$ . Chem. Mater. **2015**, 27 (8), 2812–2820.
- (2) Sui, F.; Kauzlarich, S. M. Tuning Thermoelectric Properties of Type I Clathrate  $K_{8-x}Ba_xAl_{8+x}Si_{38-x}$  through Barium Substitution. *Chem. Mater.* **2016**, 28 (9), 3099–3107.
- (3) Zaikina, J. V.; Batuk, M.; Abakumov, A. M.; Navrotsky, A.; Kauzlarich, S. M. Facile synthesis of Ba<sub>(1-x)</sub>K<sub>(x)</sub>Fe<sub>2</sub>As<sub>2</sub> superconductors via hydride route. *J. Am. Chem. Soc.* **2014**, *136* (48), 16932–9.
- (4) Schmidt, M.; Schmidt, J.; Grin, Y.; BÖhm, A.; Kieback, B.; Scholl, R.; Schubert, T.; WeissgÄrber, T.; Zumdick, M. Production of Mg<sub>2</sub>Si and Ternary Compounds Mg<sub>2</sub> (SI,E); (E = Ge, Sn, Pb and Transition Metals; <10 wt %) Made of MgH<sub>2</sub> and Silicon and the Production of Magnesium Silicide Moulded Bodies by Pulse-Plasma-Synthesis. Patent WO02083561 A2, October 24, 2002.
- (5) Yi, T. H.; Chen, S. P.; Li, S.; Yang, H.; Bux, S.; Bian, Z. X.; Katcho, N. A.; Shakouri, A.; Mingo, N.; Fleurial, J. P.; Browning, N. D.; Kauzlarich, S. M. Synthesis and characterization of Mg<sub>2</sub>Si/Si nanocomposites prepared from MgH<sub>2</sub> and silicon, and their thermoelectric properties. *J. Mater. Chem.* **2012**, 22 (47), 24805–24813.
- (6) Zhang, Y. Z.; Han, Y. H.; Meng, Q. S. The performance of Mg<sub>2</sub>Si-based thermoelectric materials prepared from MgH<sub>2</sub>. *Mater. Res. Innovations* **2015**, *19*, S1-264–S1-268.
- (7) Chen, S. P.; Zhang, X.; Fan, W. H.; Yi, T. H.; Quach, D. V.; Bux, S.; Meng, Q. S.; Kauzlarich, S. M.; Munir, Z. A. One-step low

temperature reactive consolidation of high purity nanocrystalline Mg,Si. J. Alloys Compd. 2015, 625, 251–257.

- (8) Ma, X.; Xu, F.; Atkins, T. M.; Goforth, A. M.; Neiner, D.; Navrotsky, A.; Kauzlarich, S. M. A versatile low temperature synthetic route to Zintl phase precursors: Na<sub>4</sub>Si<sub>4</sub>, Na<sub>4</sub>Ge<sub>4</sub> and K<sub>4</sub>Ge<sub>4</sub> as examples. *Dalton transactions* **2009**, No. 46, 10250–5.
- (9) Martinolich, A. J.; Neilson, J. R. Toward Reaction-by-Design: Achieving Kinetic Control of Solid State Chemistry with Metathesis. *Chem. Mater.* **2017**, 29 (2), 479–489.
- (10) Allen, K. Chlorine hydrate. J. Chem. Soc. 1959, 4131-4132.
- (11) Kasper, J. S.; Hagenmuller, P.; Pouchard, M.; Cros, C. Clathrate Structure of Silicon  $Na_8Si_{46}$  and  $Na_xSi_{136}$  (x < 11). Science 1965, 150 (3704), 1713–4.
- (12) Neiner, D.; Okamoto, N. L.; Yu, P.; Leonard, S.; Condron, C. L.; Toney, M. F.; Ramasse, Q. M.; Browning, N. D.; Kauzlarich, S. M. Synthesis and characterization of  $K_{(8-x)}(H_2)_y Si_{46}$ . *Inorg. Chem.* **2010**, 49 (3), 815–22.
- (13) Neiner, D.; Okamoto, N. L.; Condron, C. L.; Ramasse, Q. M.; Yu, P.; Browning, N. D.; Kauzlarich, S. M. Hydrogen encapsulation in a silicon clathrate type I structure: Na<sub>5.5</sub>(H2)<sub>2.15</sub>Si<sub>46</sub>: synthesis and characterization. *J. Am. Chem. Soc.* **2007**, *129* (45), 13857–62.
- (14) Christensen, M.; Johnsen, S.; Iversen, B. B. Thermoelectric clathrates of type I. *Dalton transactions* **2010**, 39 (4), 978–92.
- (15) Warrier, P.; Koh, C. A. Silicon clathrates for lithium ion batteries: A perspective. *Appl. Phys. Rev.* **2016**, 3 (4), 040805.
- (16) Kawaji, H.; Horie, H.; Yamanaka, S.; Ishikawa, M. Superconductivity in the silicon clathrate compound (Na,Ba)<sub>x</sub>Si<sub>46</sub>. *Phys. Rev. Lett.* **1995**, *74* (8), 1427–1429.
- (17) Baitinger, M.; Böhme, B.; Ormeci, A.; Grin, Y. In *The Physics and Chemistry of Inorganic Clathrates*; Nolas, G. S., Ed.; Springer Netherlands: Dordrecht, 2014; pp 35–64.
- (18) Kauzlarich, S. M.; Sui, F.; Perez, C. J. Earth Abundant Element Type I Clathrate Phases. *Materials* **2016**, *9* (9), 714.
- (19) Dolyniuk, J. A.; Owens-Baird, B.; Wang, J.; Zaikina, J. V.; Kovnir, K. Clathrate thermoelectrics. *Mater. Sci. Eng., R* **2016**, *108*, 1–46
- (20) Nozariasbmarz, A.; et al. Thermoelectric silicides: A review. *Jpn. J. Appl. Phys.* **2017**, *56* (5S1), 0SDA04.
- (21) He, Y. P.; Sui, F.; Kauzlarich, S. M.; Galli, G. Si-based Earth abundant clathrates for solar energy conversion. *Energy Environ. Sci.* **2014**, 7 (8), 2598–2602.
- (22) Chaturvedi, A.; Stefanoski, S.; Phan, M. H.; Nolas, G. S.; Srikanth, H. Table-like magnetocaloric effect and enhanced refrigerant capacity in Eu<sub>8</sub>Ga<sub>16</sub>Ge<sub>30</sub>-EuO composite materials. *Appl. Phys. Lett.* **2011**, *99* (16), 162513.
- (23) Yamanaka, S.; Enishi, E.; Fukuoka, H.; Yasukawa, M. Highpressure synthesis of a new silicon clathrate superconductor, Ba<sub>8</sub>Si<sub>46</sub>. *Inorg. Chem.* **2000**, 39 (1), 56–8.
- (24) Baran, V.; Senyshyn, A.; Karttunen, A. J.; Fischer, A.; Scherer, W.; Raudaschl-Sieber, G.; Fassler, T. F. A combined metal-halide/metal flux synthetic route towards type-I clathrates: crystal structures and thermoelectric properties of  $A_8Al_8Si_{38}$  (A = K, Rb, and Cs). *Chem. Eur. J.* **2014**, 20 (46), 15077–88.
- (25) Snyder, G. J.; Toberer, E. S. Complex thermoelectric materials. *Nat. Mater.* **2008**, 7 (2), 105–14.
- (26) Slack, G. In CRC Handbook of Thermoelectrics; CRC Press: Boca Raton, FL, 1995.
- (27) Tadano, T.; Gohda, Y.; Tsuneyuki, S. Impact of rattlers on thermal conductivity of a thermoelectric clathrate: a first-principles study. *Phys. Rev. Lett.* **2015**, *114* (9), 095501.
- (28) Lory, P.-F.; Pailhès, S.; Giordano, V. M.; Euchner, H.; Nguyen, H. D.; Ramlau, R.; Borrmann, H.; Schmidt, M.; Baitinger, M.; Ikeda, M.; Tomeš, P.; Mihalkovič, M.; Allio, C.; Johnson, M. R.; Schober, H.; Sidis, Y.; Bourdarot, F.; Regnault, L. P.; Ollivier, J.; Paschen, S.; Grin, Y.; de Boissieu, M. Direct measurement of individual phonon lifetimes in the clathrate compound Ba<sub>7.81</sub>Ge<sub>40.67</sub>Au<sub>5.33</sub>. *Nat. Commun.* **2017**, 8 (1), 491.
- (29) Euchner, H.; Pailhès, S.; Nguyen, L. T. K.; Assmus, W.; Ritter, F.; Haghighirad, A.; Grin, Y.; Paschen, S.; de Boissieu, M. Phononic

filter effect of rattling phonons in the thermoelectric clathrate  $Ba_8Ge_{40+x}Ni_{6-x}$ . Phys. Rev. B: Condens. Matter Mater. Phys. **2012**, 86 (22), 224303.

- (30) Pailhès, S.; Euchner, H.; Giordano, V. M.; Debord, R.; Assy, A.; Gomès, S.; Bosak, A.; Machon, D.; Paschen, S.; de Boissieu, M. Localization of Propagative Phonons in a Perfectly Crystalline Solid. *Phys. Rev. Lett.* **2014**, *113* (2), 025506.
- (31) Norouzzadeh, P.; Myles, C. W.; Vashaee, D. Phonon dynamics in type-VIII silicon clathrates: Beyond the rattler concept. *Phys. Rev. B: Condens. Matter Mater. Phys.* **2017**, *95* (19), 195206.
- (32) Fleurial, J. P. Thermoelectric Power Generation Materials: Technology and Application Opportunities. *JOM* **2009**, *61* (4), 79–85.
- (33) Saramat, A.; Svensson, G.; Palmqvist, A. E. C.; Stiewe, C.; Mueller, E.; Platzek, D.; Williams, S. G. K.; Rowe, D. M.; Bryan, J. D.; Stucky, G. D. Large thermoelectric figure of merit at high temperature in Czochralski-grown clathrate Ba<sub>8</sub>Ga<sub>16</sub>Ge<sub>30</sub>. *J. Appl. Phys.* **2006**, *99* (2), 023708.
- (34) Martin, J.; Wang, H.; Nolas, G. S. Optimization of the thermoelectric properties of Ba<sub>8</sub>Ga<sub>16</sub>Ge<sub>30</sub>. Appl. Phys. Lett. **2008**, 92 (22), 222110.
- (35) Kroner, R.; Peters, K.; Schnering, H. v.; Nesper, R. Inorganic Crystal Structures-Crystal structure of the clathrates K<sub>8</sub>Al<sub>8</sub>Ge<sub>38</sub> and K<sub>8</sub>Al<sub>8</sub>Sn<sub>38</sub>. Z. Kristallogr. New Crystal Structures **1998**, 213 (4), 675–676.
- (36) Schnering, H. V.; Menke, H.; Kröner, R.; Peters, E.-M.; Peters, K.; Nesper, R. Crystal structure of the clathrates Rb<sub>8</sub>In<sub>8</sub>Ge<sub>38</sub> and K<sub>8</sub>In<sub>8</sub>Ge<sub>38</sub>. Z. Kristallogr. New crystal structures **1989**, 4 (213), 673–674
- (37) Bobev, S.; Sevov, S. C. Clathrates of group 14 with alkali metals: An exploration. *J. Solid State Chem.* **2000**, *153* (1), 92–105.
- (38) Albrecht, W. M.; Goode, W. D.; Mallett, M. W. Reactions in the Niobium-Hydrogen System. J. Electrochem. Soc. 1959, 106 (11), 981–986
- (39) Petricek, V.; Dusek, M.; Palatinus, L. Crystallographic Computing System JANA2006: General features. Z. Kristallogr. Cryst. Mater. 2014, 229 (5), 345–352.
- (40) Borup, K. A.; Toberer, E. S.; Zoltan, L. D.; Nakatsukasa, G.; Errico, M.; Fleurial, J. P.; Iversen, B. B.; Snyder, G. J. Measurement of the electrical resistivity and Hall coefficient at high temperatures. *Rev. Sci. Instrum.* **2012**, *83* (12), 123902.
- (41) Hellenbrandt, M. The Inorganic Crystal Structure Database (ICSD)—Present and Future. Crystallogr. Rev. 2004, 10 (1), 17–22.
- (42) Kröner, R. Zintl-Phasen der Alkalimetalle und des Bariums mit Clathratstruktur; University of Stuttgart: Stuttgart, 1989.
- (43) Cooper, A. Precise lattice constants of germanium, aluminum, gallium arsenide, uranium, sulphur, quartz and sapphire. *Acta Crystallogr.* **1962**, *15* (6), 578–582.
- (44) Uher, C. In *Thermal Conductivity*; Tritt, T. M., Ed.; Springer US: Boston, MA, 2004; Chapter 2, pp 21–91.
- (45) Singh, S. K.; et al. Synthesis and transport properties of ternary type-I Si clathrate K<sub>8</sub>Al<sub>7</sub>Si<sub>39</sub>. *Jpn. J. Appl. Phys.* **2015**, 54 (9), 091801.
- (46) Akai, K.; Uemura, T.; Kishimoto, K.; Tanaka, T.; Kurisu, H.; Yamamoto, S.; Koyanagi, T.; Koga, K.; Anno, H.; Matsuura, M. First-Principles Study of Semiconducting Clathrate Ba<sub>8</sub>Al<sub>16</sub>Ge<sub>30</sub>. *J. Electron. Mater.* **2009**, 38 (7), 1412–1417.
- (47) Tsujii, N.; Roudebush, J. H.; Zevalkink, A.; Cox-Uvarov, C. A.; Jeffery Snyder, G.; Kauzlarich, S. M. Phase stability and chemical composition dependence of the thermoelectric properties of the type-I clathrate  $Ba_8Al_xSi_{46-x}$  (8  $\leq x \leq$  15). *J. Solid State Chem.* **2011**, 184 (5), 1293–1303.
- (48) May, A.; Snyder, G. Introduction to Modeling Thermoelectric Transport at High Temperatures. *Materials, Preparation, and Characterization in Thermoelectrics*; CRC Press: Boca Raton, FL, 2012; p 1–18.
- (49) Toberer, E. S.; Brown, S. R.; Ikeda, T.; Kauzlarich, S. M.; Jeffrey Snyder, G. High thermoelectric efficiency in lanthanum doped Yb<sub>14</sub>MnSb<sub>11</sub>. Appl. Phys. Lett. **2008**, 93 (6), 062110.

(50) Toberer, E. S.; May, A. F.; Snyder, G. J. Zintl Chemistry for Designing High Efficiency Thermoelectric Materials. *Chem. Mater.* **2010**, 22 (3), 624–634.

- (51) May, A. F.; Fleurial, J.-P.; Snyder, G. J. Optimizing Thermoelectric Efficiency in  $La_{3-x}Te_4$  via Yb Substitution. *Chem. Mater.* **2010**, 22 (9), 2995–2999.
- (52) Toberer, E. S.; May, A. F.; Melot, B. C.; Flage-Larsen, E.; Snyder, G. J. Electronic structure and transport in thermoelectric compounds AZn<sub>2</sub>Sb<sub>2</sub> (A = Sr, Ca, Yb, Eu). *Dalton transactions* **2010**, 39 (4), 1046–54.
- (53) Liao, P.; Spear, K.; Massalski, T. Binary alloy phase diagrams; ASM International: Materials Park, Ohio, 1990; Vol. 1, pp 557–559.
- (54) Yang, H.; Shu, G.; Tian, H.; Ma, X.; Chen, T.; Liu, P. Optimization of thermoelectric generator (TEG) integrated with three-way catalytic converter (TWC) for harvesting engine's exhaust waste heat. *Appl. Therm. Eng.* **2018**, *144*, 628–638.
- (55) LeBlanc, S. Thermoelectric generators: Linking material properties and systems engineering for waste heat recovery applications. Sustainable Materials and Technologies 2014, 1–2, 26–35.